

# Exploring Peptide Bond Formation Using Transition State Search and Wave Packet Dynamics

Published as part of *The Journal of Physical Chemistry Letters* special issue “Wei-Hai Fang Festschrift”.

Sarah Ghazanfari, Yulun Han, Amara Arshad, Wenjie Xia,\* Svetlana Kilina,\* and Dmitri Kilin\*

Cite This: *J. Phys. Chem. Lett.* 2025, 16, 6968–6974

Read Online

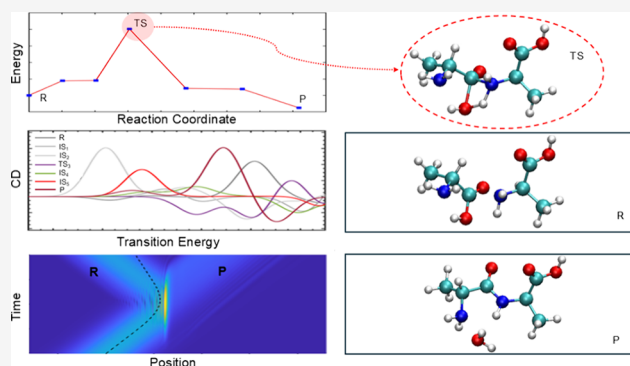
ACCESS |

Metrics & More

Article Recommendations

Supporting Information

**ABSTRACT:** This first-principles study investigates the interactions between amino acids and various types of montmorillonite clay surfaces, including a pristine surface, a surface with an oxygen vacancy, a surface with a silicon vacancy, and an Fe-doped surface. Our results show that all clay surfaces exhibit negative binding energies, indicating that the interaction between clay and amino acids is thermodynamically favorable. Among them, the surface with a Si vacancy displays the most negative binding energy, corresponding to the strongest interaction. We also examine the reactions between two alanine molecules to form a dipeptide molecule through the elimination of a water molecule in the absence of clay surfaces. The transition state search suggests that a proton transfer plays a critical role in the peptide bond formation based on structural and energetic features observed along the reaction path. Circular dichroism spectra computed for reactant, intermediate, and product states show distinct chiral signatures. Wave packet dynamics calculations indicate that quantum tunneling might be the mechanism underlying the reduced activation energy at low temperatures. These findings offer insight into the physicochemical processes at clay–amino acid interfaces and support the design of clay-based materials with applications in biotechnology and prebiotic chemistry.



Adsorption of biomolecules onto mineral surfaces<sup>1–4</sup> has attracted increasing attention in recent years due to its broad implications in materials science,<sup>5</sup> biocatalysis,<sup>6–8</sup> and prebiotic chemistry.<sup>9</sup> In particular, clay minerals have emerged as compelling platforms for studying interfacial phenomena owing to their high surface area, structural heterogeneity, and tunable surface chemistry.<sup>9</sup> Among them, montmorillonite (MMT),<sup>10–12</sup> a 2:1 smectite clay composed of layered tetrahedral–octahedral–tetrahedral sheets,<sup>13</sup> has been widely studied due to its unique physicochemical properties and its role as a model material for adsorption and catalysis studies. The weak van der Waals interactions that hold these layers together<sup>14</sup> and the isomorphic substitutions within the layers give rise to a net negative charge, which is typically balanced by exchangeable interlayer cations, such as Na<sup>+</sup>, Mg<sup>2+</sup>, or Fe<sup>3+</sup>.<sup>13,15–17</sup> These characteristics provide a favorable environment for the adsorption and potential chemical transformation of small biomolecules, such as amino acids.<sup>18,19</sup> Mineral surfaces could serve as catalysts for biomolecular polymerization.<sup>20</sup> Clay minerals can concentrate, stabilize, and even activate biomolecular building blocks under various geochemical conditions.<sup>21–23</sup> For example, dry-wet cycles<sup>21,23</sup> have been shown to facilitate peptide bond formation for amino acids adsorbed on clay surfaces. Peptide bond formation

is a fundamental biochemical process. It involves the formation of an amide group in a dipeptide through the elimination of water and condensation of two amino acids.<sup>24</sup> Experimental and theoretical investigations<sup>25–31</sup> suggest that amino acids interact with clays through a combination of electrostatic attraction, hydrogen bonding, van der Waals forces, and, in some cases, coordination with metal ions present in the clay matrix. These interactions are modulated by environmental parameters, such as pH, temperature, and ionic strength, highlighting the complex nature of biomolecule–clay interfaces.<sup>32</sup>

Despite several published observations,<sup>1,5,33–35</sup> a detailed mechanistic understanding of how structural variations in clay minerals influence biomolecular adsorption and reactivity remains incomplete. Density functional theory (DFT)<sup>36–41</sup> can be used to calculate the interaction energies, electron

Received: April 10, 2025

Revised: June 11, 2025

Accepted: June 12, 2025

distributions, and potential energy surfaces (PESs) associated with biomolecule–surface interactions. A DFT-based transition state search<sup>42,43</sup> allows for the identification of reaction pathways and the estimation of activation barriers, offering insight into the feasibility of surface-mediated chemical transformations. Spin-polarized DFT calculations enable the study of clay minerals containing paramagnetic centers with enhanced surface reactivity.<sup>44</sup>

Here, we investigate the molecular-level interactions between amino acids and MMT surfaces. The amino acid is a dipeptide molecule formed between two alanine molecules. Alanine is a simple amino acid with well-characterized behaviors and has been used as a model in protein folding.<sup>45,46</sup> We consider various types of surfaces, including a pristine surface, a surface with an oxygen vacancy (MMT-V<sub>O</sub>), a surface with a silicon vacancy (MMT-V<sub>Si</sub>), and an Fe-doped surface (Fe-MMT). For Fe-MMT, we consider the high spin (HS) state, as it shows the lowest total energy compared to the other spin states according to our previous work.<sup>47</sup> We also examine the reactions between two alanine molecules to form the dipeptide molecule in the absence of clay surfaces.

DFT calculations were carried out with the Vienna *Ab initio* Simulation Package (VASP)<sup>48</sup> using the Perdew–Burke–Ernzerhof (PBE)<sup>49</sup> exchange–correlation functional. Spin-polarized DFT + U<sup>50</sup> calculations were performed for Fe-doped slabs to account for the 3d electrons, whereas spin-restricted DFT calculations were employed for the other systems. Binding energies ( $E_b$ ) were calculated for all slabs with the adsorbates. We also implemented the climbing image nudged elastic band (CI-NEB) method<sup>51–53</sup> to identify reaction pathways between two alanine molecules to form a dipeptide molecule in the absence of MMT surfaces. Wave packet dynamics<sup>54</sup> was used to investigate quantum tunneling effects across the reaction barrier. Activation energies were derived using a modified Arrhenius<sup>55–58</sup> approach fitted to temperature-dependent reaction rate constants. Atomic models were constructed using a pyrophyllite-based MMT structure with the formula of  $\text{Al}_2\text{Si}_4\text{O}_{10}(\text{OH})_2$ . A  $2 \times 2 \times 1$  supercell was constructed by replicating the unit cell. Periodic boundary conditions were applied in the  $x$ ,  $y$ , and  $z$  directions. A vacuum layer of 10 Å was added in the  $z$  direction to minimize spurious interactions. Clay models with vacancies were constructed by removing one oxygen or silicon atom from the surface layer. For the Fe-MMT model, one Al atom was replaced by one Fe atom, corresponding to the impurity concentration of 12.5%. A dipeptide molecule along with a water molecule were adsorbed per surface. Additional computational details are provided in the Supporting Information.

Figure 1 shows the geometry-optimized structures for various models. Based on the optimized structures, binding energies are calculated as  $E_b = E_{\text{A@S}} - E_{\text{S}} - E_{\text{A}}$ , where  $E_{\text{A@S}}$  is the total energy of the MMT slab with an adsorbate,  $E_{\text{S}}$  is the total energy of the clean slab, and  $E_{\text{A}}$  is the total energy of isolated adsorbate molecules. The binding energies represent the interaction energy between adsorbates and respective clay surfaces rather than values normalized per atom. These binding energies are derived from total electronic energies, referred to here as total energies, calculated at 0 K using DFT, without thermal, vibrational, or entropic corrections. The calculated binding energies are  $-0.66$ ,  $-0.64$ ,  $-1.58$ , and  $-0.48$  eV for pristine MMT, MMT-V<sub>O</sub>, MMT-V<sub>Si</sub>, and Fe-MMT, respectively (see Figure 1). All clay surfaces exhibit negative binding energies, indicating that the interaction between clay and

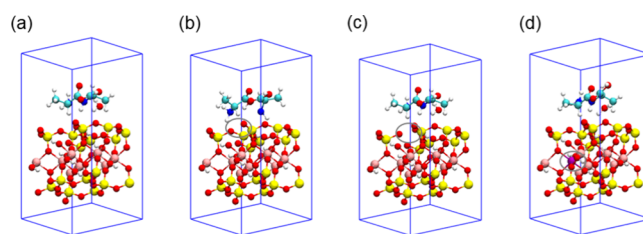


**Figure 1.** Optimized geometries of various clay structures with adsorbates. Panels a, b, c, and d correspond to pristine MMT, MMT-V<sub>O</sub>, MMT-V<sub>Si</sub>, and Fe-MMT, respectively. White spheres represent H; cyan spheres represent C; blue spheres represent N; red spheres represent O; yellow spheres represent Si; pink spheres represent Al; and magenta spheres represent Fe.

amino acids is thermodynamically favorable. Among them, the surface with a Si vacancy displays the most negative binding energy, corresponding to the strongest interaction. The summary of binding energies for various systems is reported in Table S1. Note that the commonly reported binding energies for physisorption range from 0 to  $-0.41$  eV.<sup>59</sup> This indicates chemisorption for the slab with a Si vacancy and physisorption for the other slabs.

We also conducted Bader charge analysis<sup>60</sup> for various MMT slabs with adsorbates (see Table S2). The slabs exhibit positive Bader charge values, while the adsorbates show negative values, indicating electron transfer from the adsorbates to the slabs. For MMT-V<sub>Si</sub>, roughly 0.75 e is transferred from the adsorbate to the slab, which is characteristic of chemisorption. In contrast, the other slabs exhibit only a negligible charge transfer, consistent with physisorption. Thus, the Bader charge analysis supports our interpretation based on binding energy results.

Adsorption of amino acids on clay minerals alters electronic properties, often shifting energy levels and modifying the bandgaps. Figure S1 shows the density of states (DOS) of various slabs with adsorbates. Fe-MMT shows the smallest HOMO–LUMO gap (between the highest occupied molecular orbital and the lowest unoccupied molecular orbital) due to Fe 3d orbital contributions, consistent with studies showing that transition metal doping introduces midgap states and enhances conductivity.<sup>61</sup> Surface defects also affect electronic structures. MMT-V<sub>O</sub> exhibits a smaller gap than MMT-V<sub>Si</sub>, indicating that oxygen atoms play a greater role in defining the clay's band structures. Their absence leads to the appearance of localized states within the gap. In contrast, the MMT-V<sub>Si</sub> model exhibits the largest gap. This large gap can be attributed to the structural role of silicon atoms, which, while critical for the clay framework, contribute less directly to electronic states near the Fermi level. As a result, removing a Si atom introduces fewer midgap states compared to oxygen vacancies or transition metal dopants, leading to a broader energy separation between HOMO and LUMO.

We then investigated the peptide bond formation of isolated alanine molecules in the absence of clay surfaces. The reaction pathway, transition state geometry, and barrier height are determined from CI-NEB calculations (see Figure 2). The reported mechanisms of peptide bond formation under gas-phase and solvated conditions involves carbonyl carbon of one alanine molecule undergoing nucleophilic attack by amino nitrogen of another.<sup>62</sup> Our results show that, along the reaction pathway, the amino group of one alanine gradually approaches the carboxyl group of the other. At the transition state, a four-

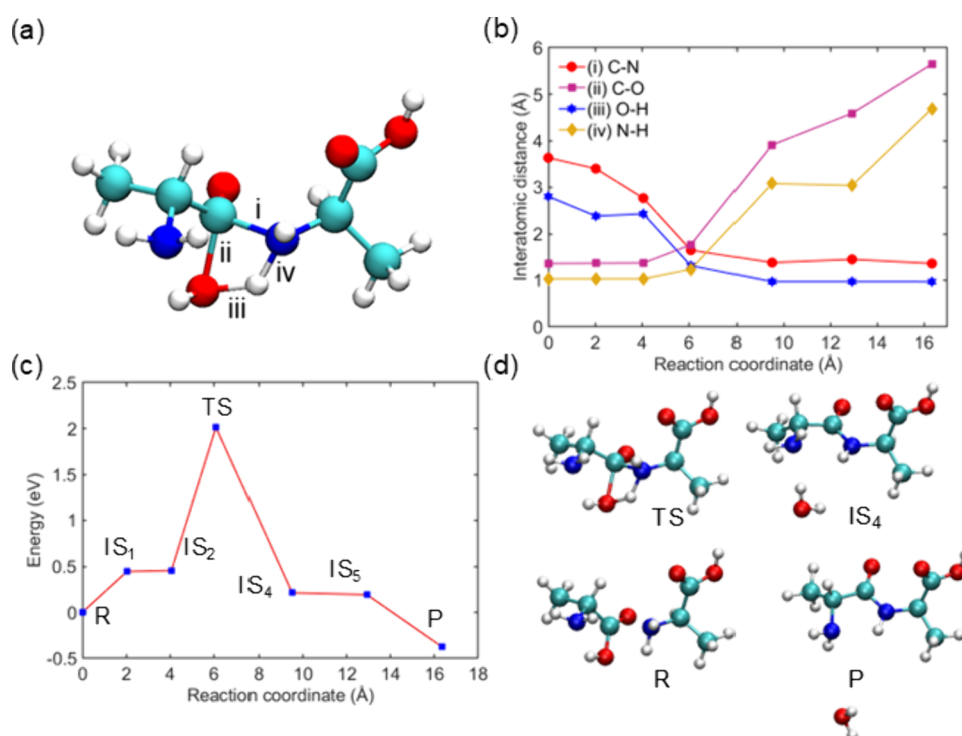


**Figure 2.** Peptide bond formation of isolated alanine molecules in the absence of clay surfaces from CI-NEB calculations. (a) Transition state geometry with labels for selected interatomic distances. (b) Interatomic distances along the reaction path. (c) Minimum energy path leading to the formation of a dipeptide molecule through the elimination of a water molecule. R, IS, TS, and P represent the reactant, intermediate, transition, and product states, respectively. (d) Geometries of representative structures along the reaction pathway.

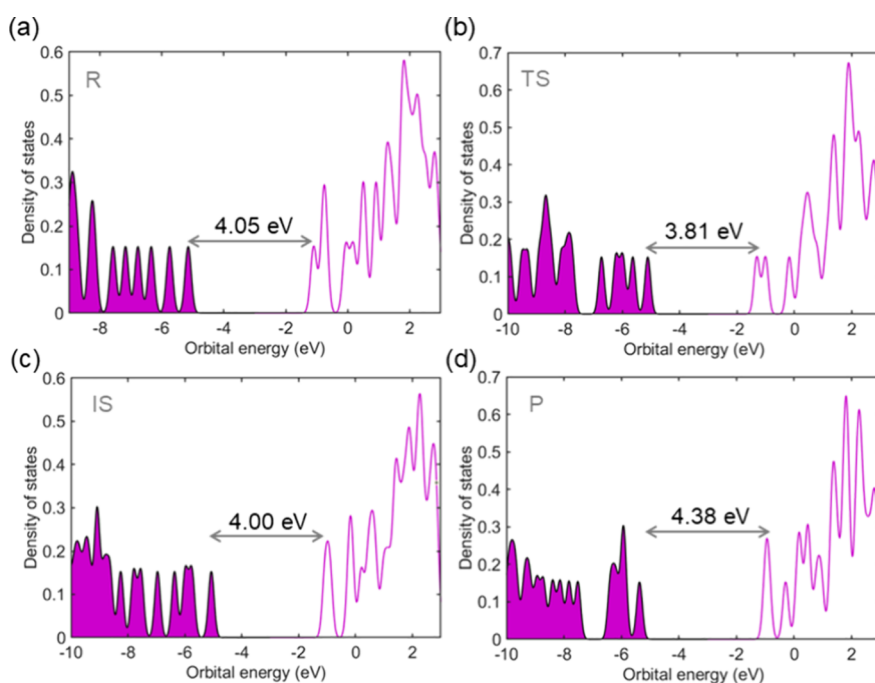


**Figure 3.** Density of states for the (a) reactant, (b) transition state, (c) representative intermediate, and (d) product along the peptide formation pathway. The labels indicate HOMO–LUMO gaps. The magenta shaded areas correspond to occupied states, while the unfilled areas correspond to unoccupied states.

membered ring is formed, consisting of nitrogen and hydrogen from the amino group and carbon and hydroxyl oxygen from the carboxyl group. The interatomic distance between hydrogen and oxygen is 1.32 Å, whereas the interatomic distance between hydrogen and nitrogen is 1.24 Å. This

hydrogen has a Bader charge of  $-0.54$  e. The negative Bader charge value means that the species is donating electrons, suggesting that the species being transferred is a proton rather than a hydrogen radical. As the reaction progresses, the four-membered ring breaks as the proton transfers to hydroxyl

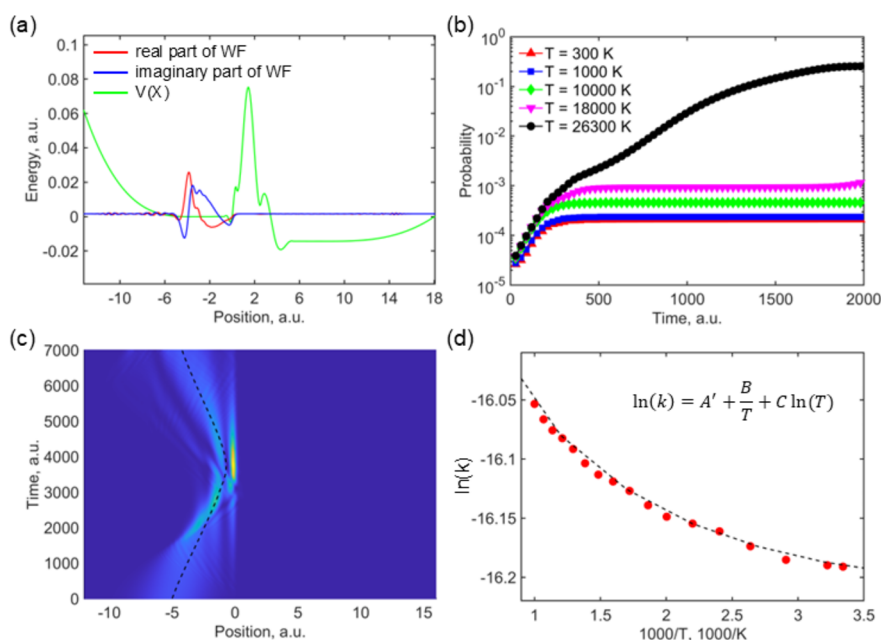


**Figure 4.** Wave packet dynamics for the peptide bond formation of isolated alanine molecules in the absence of clay surfaces. (a) Snapshot of the wave packet dynamics at 300 K.  $V(x)$ , the PES, is based on results from CI-NEB calculations. (b) Probability of product formation versus time at various temperatures. (c) Wave packet dynamics as a function of position and time at 300 K. The dashed line represents the expectation value. The blue colors represent low-intensity values, while the yellow colors represent high-intensity values. (d) Calculated rate constants versus temperatures (red circles) and the fitting (black dashed line) by a modified Arrhenius equation with  $A' = -17.35$ ,  $B = 35.85$ , and  $C = 0.18$ .

oxygen, leading to the release of a water molecule. The distance between the carbon and nitrogen atoms decreases, ultimately resulting in the formation of a peptide bond. At the transition state, hydrogen is positioned nearly equidistant between the nitrogen and oxygen atoms, creating a symmetric potential energy barrier. This configuration suggests the possibility of quantum tunneling, as hydrogen, due to its low mass, can traverse the energy barrier through quantum mechanical effects rather than overcoming it classically.<sup>54</sup> It is worth noting that, although MMT has been experimentally implicated in promoting peptide bond formation and polymerization<sup>21,23</sup> under prebiotic conditions, we did not model the reaction pathways on MMT surfaces in the current study. Instead, the surface interaction results presented here focus on the binding behavior of the product state (a dipeptide molecule and a water molecule) of the peptide formation reaction on various MMT surface models. The peptide bond formation pathway is provided as a mechanistic reference for future studies that may investigate surface-mediated reactivity more directly.

Partial charge densities for HOMO and LUMO of reactant, representative intermediate, and product states can be seen in Figure S2. In the reactant state, the HOMO is primarily localized on one of the alanine molecules. As the reaction proceeds, the HOMO gradually shifts to the other alanine, where it remains after peptide bond formation in the resulting dipeptide. The LUMO is initially delocalized over both alanine molecules with a dominant contribution from the same alanine as the HOMO in the reactant state. As the reaction progresses, the minor LUMO contribution from the second alanine decreases. In the final dipeptide, the HOMO and LUMO become spatially separated, each localized on different parts of the molecule. This evolution of charge density highlights the redistribution of frontier molecular orbitals during peptide bond formation. The shifting HOMO indicates a change in

nucleophilic character between the monomers, while the final separation of HOMO and LUMO in the product reflects the formation of a more electronically stable, less reactive molecular system.

The barrier height is about 2.04 eV. Once the barrier is overcome, the peptide bond forms, replacing weaker non-bonded interactions with stronger covalent bond. This bond is further stabilized by resonance delocalization, which imparts a partial double-bond character to the C–N linkage. As a result, the product has a lower overall potential energy than the reactant, making the reaction exothermic (Figure 2c). Our CI-NEB calculations focus on neutral alanine molecules, corresponding to gas-phase conditions. In aqueous or polar environments, however, alanine exists in its zwitterionic form ( $-\text{NH}_3^+$  and  $-\text{COO}^-$ ),<sup>63,64</sup> which could alter reactivity, transition state geometry, and barrier height by enhancing electrostatic interactions or modifying nucleophilicity.

DOS is computed for the reactant, transition state, representative intermediate, and product along the reaction pathway, as shown in Figure 3. The transition state structure shows the smallest HOMO–LUMO gap of 3.81 eV, indicating a highly reactive electronic configuration. The reactant and intermediate states exhibit slightly larger gaps of 4.05 and 4.00 eV, respectively, while the final product has the widest gap of 4.38 eV, reflecting its enhanced electronic stability. In addition to the gap size, the DOS profiles reveal differences in the shape and distribution of states near the Fermi level. The reactant shows broader peaks near LUMO, suggesting a delocalized electron density and higher reactivity. As the system progresses to the product, the states become more localized and sharply defined, indicating reduced reactivity and a more stable closed-shell configuration. The absence of midgap states and the widening energy separation from HOMO to LUMO further support that the product and intermediate are less electronically reactive than the initial reactant. Overall, the DOS

evolution across the reaction sequence aligns with the expected electronic reorganization during peptide bond formation and highlights a clear trend from reactive to stable configurations.

To further elucidate reaction mechanisms, we computed circular dichroism (CD) spectra<sup>65,66</sup> for reactant, intermediate, and product states along the reaction pathways. We also computed CD spectra for L- and D-alanine, which are mirror images of each other. Note that, throughout this paper, the alanine model refers to L-alanine unless explicitly stated otherwise. Simulated CD spectra (Figure S3) of various structures along the reaction pathways show distinct chiral shifts, reflecting structural changes in the chiral environment during the peptide bond formation. The correspondence between CD spectral variations and key geometrical changes (e.g., bond formation and proton transfer) reinforces the interpretation of the transition state structure as a highly dynamic stereochemically sensitive point along the reaction coordinate. Notably, mixing D- and L-alanine leads to a reduction in the CD signal intensity, indicating a loss of overall chiral coherence in the system. This observation suggests that stereochemical purity may influence the reaction efficiency, highlighting the importance of chirality in peptide-forming pathways. Thus, CD spectroscopy offers an independent spectroscopic validation of the transition state features observed in structural and energetic analyses and deepens our understanding of how chirality influences peptide-forming mechanisms.

CI-NEB calculations provide us with a minimum energy path between reactant and product states on a PES for the peptide bond formation reaction. However, CI-NEB is a classical method and cannot describe quantum effects, such as zero-point energy, tunneling, and wave function delocalization, which might be important for light atoms, such as hydrogen, due to uncertainty in position and momentum. Here, we carried out nuclear wave packet dynamics calculations to quantify the degrees of freedom related to hydrogen motion. The procedure of wave packet dynamics calculations can be found in ref 54, which was published by some of us. The modeled reactions focus on proton transfer, incorporating quantum corrections to proton translational motion during collisions. The calculations at 300 K (panels a and c of Figure 4) show the Gaussian wave packet evolving along the PES (0.0–5.3 au of length), which is obtained from CI-NEB calculations. Our results show the splitting of the wave packet, indicating that part of it passes through the PES to form the product, while the other part is reflected, preserving as the reactant. The splitting confirms quantum superposition effects. As shown in Figure 4b, product formation probability increases with the temperature. Initially, tunneling probability rises linearly with time and then plateaus (>200 au of time) as the system reaches a steady state. At an extremely high temperature, the probability jumps to 0.1, highlighting the role of thermal energy in enhancing tunneling.<sup>67</sup>

The high-temperature wave packet dynamics calculations reflect extreme conditions and bridge classical and quantum reaction dynamics.<sup>68</sup> A modified Arrhenius fit (Figure 4d) yields activation energies  $\tilde{E}_a(T)$  from  $\sim 0.0077$  eV (300 K) to  $\sim 0.022$  eV (1000 K), significantly lower than the classical value of 2.04 eV, indicating strong tunneling contributions. Despite low reaction yields, these low barriers suggest that tunneling-driven pathways may dominate under high-energy conditions.<sup>69</sup> However, factors such as reactant availability and competing pathways can still limit the overall efficiency. Details

about the wave packet dynamics, such as wave packet propagation scheme and activation energy, are provided in the Supporting Information.

In summary, this study provides insight into the adsorption of amino acids on various MMT clay surfaces, including a pristine surface, a surface with an oxygen vacancy, a surface with a silicon vacancy, and an Fe-doped surface. All clay surfaces exhibit negative binding energies, indicating that the interaction between clay and amino acids is thermodynamically favorable. Among them, the surface with a Si vacancy displays the most negative binding energy, corresponding to the strongest interaction. The surface with a Si vacancy shows characteristics of chemisorption, whereas the other surfaces show characteristics of physisorption, highlighting the catalytic potential of these interfaces. We also investigate the peptide bond formation of isolated alanine molecules in the absence of clay surfaces. Our results show a barrier height of about 2.04 eV and that, at the transition state, a four-membered ring is formed, consisting of N and H from the amino group of one alanine and C and hydroxyl O from the carboxyl group of the other alanine. We also calculate electronic structures and CD spectra for reactant, intermediate, and product states along the reaction pathways and found distinct features for each structure. This reinforces the interpretation of the transition state structure as a highly dynamic, stereochemically sensitive point along the reaction coordinate. Complementary wave packet dynamics indicates that quantum tunneling contributes to reduced activation energies, which could be a key consideration for understanding reaction kinetics under prebiotic or thermodynamically mild conditions. These findings are expected to advance the fundamental understanding of biomolecule–clay interactions and offer practical insights for designing clay-based catalytic systems.

## ■ ASSOCIATED CONTENT

### Supporting Information

The Supporting Information is available free of charge at <https://pubs.acs.org/doi/10.1021/acs.jpcllett.5c01096>.

Computational details, DOS for optimized models, partial charge distributions for HOMO and LUMO of reactant, representative intermediate, and product states along the peptide bond formation reaction, CD spectra for various structures along the reaction and L- and D-alanine, and calculated binding energy and Bader charges for various models (PDF)

## ■ AUTHOR INFORMATION

### Corresponding Authors

Wenjie Xia – Department of Aerospace Engineering, Iowa State University, Ames, Iowa 50011, United States; [orcid.org/0000-0001-7870-0128](https://orcid.org/0000-0001-7870-0128); Email: [wxia@iastate.edu](mailto:wxia@iastate.edu)

Svetlana Kilina – Department of Chemistry and Biochemistry, North Dakota State University, Fargo, North Dakota 58108, United States; [orcid.org/0000-0003-1350-2790](https://orcid.org/0000-0003-1350-2790); Email: [svetlana.kilina@ndsu.edu](mailto:svetlana.kilina@ndsu.edu)

Dmitri Kilin – Department of Chemistry and Biochemistry, North Dakota State University, Fargo, North Dakota 58108, United States; [orcid.org/0000-0001-7847-5549](https://orcid.org/0000-0001-7847-5549); Email: [dmitri.kilin@ndsu.edu](mailto:dmitri.kilin@ndsu.edu)

## Authors

Sarah Ghazanfari – Department of Civil, Construction, and Environmental Engineering and Department of Chemistry and Biochemistry, North Dakota State University, Fargo, North Dakota 58108, United States; Advanced Research Computing, Virginia Tech, Blacksburg, Virginia 24061, United States; [orcid.org/0000-0003-4777-3070](https://orcid.org/0000-0003-4777-3070)

Yulun Han – Department of Chemistry and Biochemistry, North Dakota State University, Fargo, North Dakota 58108, United States; Department of Natural Sciences, Texas A&M University—San Antonio, San Antonio, Texas 78224, United States; [orcid.org/0000-0002-8619-0233](https://orcid.org/0000-0002-8619-0233)

Amara Arshad – Department of Civil, Construction, and Environmental Engineering, North Dakota State University, Fargo, North Dakota 58108, United States

Complete contact information is available at:

<https://pubs.acs.org/10.1021/acs.jpcllett.5c01096>

## Notes

The authors declare no competing financial interest.

## ACKNOWLEDGMENTS

Sarah Ghazanfari, Amara Arshad, and Wenjie Xia acknowledge the support from the National Science Foundation (NSF) under NSF CMMI Award 2331017. Svetlana Kilina thanks NSF EPSCoR RII Track-1: ND-ACES Grant 1946202 for partial financial support to carry out this work. Sarah Ghazanfari acknowledges the ND-ACES Doctoral STEM Teaching Assistantship Award from ND EPSCoR. Dmitri Kilin acknowledges NSF Award 1944921 for developing methods of quantum dynamics and NSF Award 2004197 for developing methods for the description of charge transfer. The U.S. Department of Energy, DE-SC0022239, for research of light emitters based on earth-abundant metals is acknowledged by the authors. This work used supercomputing resources of the DOE BES NERSC facility. The authors thank Dinesh Thapa, David Graupner, Landon Johnson, Meade Erickson, Hadassah Griffin, William Tupa, and Joseph Granlie for their editorial suggestions. This work was performed, in part, at the Center for Integrated Nanotechnologies, an Office of Science User Facility operated for the U.S. Department of Energy (DOE) Office of Science by Los Alamos National Laboratory (Contract 89233218CNA000001) and Sandia National Laboratories (Contract DE-NA-0003525).

## REFERENCES

- (1) Moro, D.; Ulian, G.; Valdrè, G. Amino Acids-Clay Interaction at the Nano-Atomic Scale: The L-Alanine-Chlorite System. *Appl. Clay Sci.* **2019**, *172*, 28–39.
- (2) Aquino, A. J. A.; Tunega, D.; Gerzabek, M. H.; Lischka, H. Modeling Catalytic Effects of Clay Mineral Surfaces on Peptide Bond Formation. *J. Phys. Chem. B* **2004**, *108* (28), 10120–10130.
- (3) Zhu, C.; Wang, Q.; Huang, X.; Yun, J.; Hu, Q.; Yang, G. Adsorption of Amino Acids at Clay Surfaces and Implication for Biochemical Reactions: Role and Impact of Surface Charges. *Colloids Surfaces B Biointerfaces* **2019**, *183*, No. 110458.
- (4) Contreras-Torres, F. F.; Basiuk, V. A. Imidazo [1,2-*a*]Pyrazine-3, 6-Diones Derived from  $\alpha$ -Amino Acids: A Theoretical Mechanistic Study of Their Formation via Pyrolysis and Silica-Catalyzed Process. *J. Phys. Chem. A* **2006**, *110* (23), 7431–7440.
- (5) Mignon, P.; Ugliengo, P.; Sodupe, M. Theoretical Study of the Adsorption of RNA/DNA Bases on the External Surfaces of Na<sup>+</sup>-Montmorillonite. *J. Phys. Chem. C* **2009**, *113* (31), 13741–13749.

- (6) Bain, C. D.; Evans, S. D. Laying It on Thin. *Chem. Br.* **1995**, *31* (1), 46–48.
- (7) Donhauser, Z. J.; Mantooth, B. A.; Kelly, K. F.; Bumm, L. A.; Monnell, J. D.; Stapleton, J. J.; Price, D. W.; Rawlett, A. M.; Allara, D. L.; Tour, J. M.; Weiss, P. S. Conductance Switching in Single Molecules through Conformational Changes. *Science* **2001**, *292* (5525), 2303–2307.
- (8) Hentze, H.-P.; Antonietti, M. Porous Polymers and Resins for Biotechnological and Biomedical Applications. *Rev. Mol. Biotechnol.* **2002**, *90* (1), 27–53.
- (9) Bernal, J. D. The Physical Basis of Life. *Proc. Phys. Soc. Sect. B* **1949**, *62* (10), 597.
- (10) Ghazanfari, S.; Alesadi, A.; Liao, Y.; Zhang, Y.; Xia, W. Molecular Insights into the Temperature and Pressure Dependence of Mechanical Behavior and Dynamics of Na-Montmorillonite Clay. *Nanoscale Adv.* **2023**, *5* (20), 5449–5459.
- (11) Ghazanfari, S.; Faisal, H. M. N.; Katti, K. S.; Katti, D. R.; Xia, W. A Coarse-Grained Model for the Mechanical Behavior of Na-Montmorillonite Clay. *Langmuir* **2022**, *38* (16), 4859–4869.
- (12) Nie, W.; Liao, Y.; Ghazanfari, S.; Wang, Y.; Wang, X.; Huang, Y.; Xia, W. Insights into the Thermomechanical and Interfacial Behaviors of Polymer-clay Nanocomposites via Coarse-grained Molecular Dynamics Simulations. *Polym. Compos.* **2024**, *45* (9), 8508–8526.
- (13) Bergaya, F.; Lagaly, G. General Introduction: Clays, Clay Minerals, and Clay Science. *Dev. clay Sci.* **2006**, *1*, 1–18.
- (14) Akalin, E.; Akyuz, S.; Akyuz, T. Adsorption and Interaction of 5-Fluorouracil with Montmorillonite and Saponite by FT-IR Spectroscopy. *J. Mol. Struct.* **2007**, *834*, 477–481.
- (15) Jha, A.; Garade, A. C.; Shirai, M.; Rode, C. V. Metal Cation-Exchanged Montmorillonite Clay as Catalysts for Hydroxyalkylation Reaction. *Appl. Clay Sci.* **2013**, *74*, 141–146.
- (16) Zhang, D.; Zhou, C.-H.; Lin, C.-X.; Tong, D.-S.; Yu, W.-H. Synthesis of Clay Minerals. *Appl. Clay Sci.* **2010**, *50* (1), 1–11.
- (17) Uddin, F. Montmorillonite: An Introduction to Properties and Utilization. In *Current Topics in the Utilization of Clay in Industrial and Medical Applications*; Zoveidavianpoor, M., Ed.; IntechOpen: London, U.K., 2018; DOI: 10.5772/intechopen.77987.
- (18) Fernando, A.; Khan, D.; Hoffmann, M. R.; Çakır, D. Exploring the Biointerfaces: Ab Initio Investigation of Nano-Montmorillonite Clay, and Its Interaction with Unnatural Amino Acids. *Phys. Chem. Chem. Phys.* **2023**, *25* (43), 29624–29632.
- (19) Thapa, D.; Westra, S.; Oas, V.; Kilin, D.; Kilina, S. Tunable Magnetic Order in Fe-Mg Codoped Montmorillonite Nanoclay Interfaced with Amino Acids. *ACS omega* **2025**, *10* (3), 2539–2552.
- (20) Bernal, J. D. *The Physical Basis of Life*; Routledge and Paul: London, U.K., 1951.
- (21) Ferris, J. P.; Hill, A. R., Jr.; Liu, R.; Orgel, L. E. Synthesis of Long Prebiotic Oligomers on Mineral Surfaces. *Nature* **1996**, *381* (6577), 59–61.
- (22) Hazen, R. M.; Papineau, D.; Bleeker, W.; Downs, R. T.; Ferry, J. M.; McCoy, T. J.; Sverjensky, D. A.; Yang, H. Mineral Evolution. *Am. Mineral.* **2008**, *93* (11–12), 1693–1720.
- (23) Ertem, G. Montmorillonite, Oligonucleotides, RNA and Origin of Life. *Orig. Life Evol. Biosph.* **2004**, *34*, 549–570.
- (24) Berg, J. M.; Tymoczko, J. L.; Stryer, L. *Biochemistry (Loose-Leaf)*; Macmillan: New York, 2007.
- (25) *Fundamentals of Multiscale Modeling of Structural Materials*; Xia, W., Pestana, L. A. R., Eds.; Elsevier: Amsterdam, Netherlands, 2022; DOI: 10.1016/C2019-0-04994.
- (26) Velázquez-Campoy, A.; Ohtaka, H.; Nezami, A.; Muzammil, S.; Freire, E. Isothermal Titration Calorimetry. *Curr. Protoc. Cell Biol.* **2004**, *23* (1), 17–18.
- (27) Freire, E.; Mayorga, O. L.; Straume, M. Isothermal Titration Calorimetry. *Anal. Chem.* **1990**, *62* (18), 950A–959A.
- (28) Falconer, R. J. Applications of Isothermal Titration Calorimetry—the Research and Technical Developments from 2011 to 2015. *J. Mol. Recognit.* **2016**, *29* (10), 504–515.

- (29) Erickson, M.; Han, Y.; Rasulev, B.; Kilin, D. Molecular Dynamics Study of the Photodegradation of Polymeric Chains. *J. Phys. Chem. Lett.* **2022**, *13* (19), 4374–4380.
- (30) Alesadi, A.; Xia, W.; Kilin, D. Photo-Induced Charge Transfer of Fullerene and Non-Fullerene Conjugated Polymer Blends via Ab Initio Excited-State Dynamics. *J. Phys. Chem. C* **2022**, *126* (29), 12015–12024.
- (31) Liao, Y.; Li, Z.; Ghazanfari, S.; Fatima; Croll, A. B.; Xia, W. Understanding the Role of Self-Adhesion in Crumpling Behaviors of Sheet Macromolecules. *Langmuir* **2021**, *37* (28), 8627–8637.
- (32) Kalra, S.; Pant, C. K.; Pathak, H. D.; Mehata, M. S. Studies on the Adsorption of Peptides of Glycine/Alanine on Montmorillonite Clay with or without Co-Ordinated Divalent Cations. *Colloids Surfaces A Physicochem. Eng. Asp.* **2003**, *212* (1), 43–50.
- (33) Lambert, J.-F. Adsorption and Polymerization of Amino Acids on Mineral Surfaces: A Review. *Orig. Life Evol. Biosph.* **2008**, *38*, 211–242.
- (34) Kasprzhitskii, A.; Lazorenko, G.; Kharytonau, D. S.; Osipenko, M. A.; Kasach, A. A.; Kurilo, I. I. Adsorption Mechanism of Aliphatic Amino Acids on Kaolinite Surfaces. *Appl. Clay Sci.* **2022**, *226*, No. 106566.
- (35) Baba, A. A.; Ibrahim, A. S.; Bale, R. B.; Adekola, F. A.; Alabi, A. G. F. Purification of a Nigerian Talc Ore by Acid Leaching. *Appl. Clay Sci.* **2015**, *114*, 476–483.
- (36) Kohn, W.; Sham, L. J. Self-Consistent Equations Including Exchange and Correlation Effects. *Phys. Rev.* **1965**, *140* (4A), A1133–A1138.
- (37) Jensen, F. An Introduction to the State of the Art in Quantum Chemistry. *Annu. Rep. Comput. Chem.* **2005**, *1*, 3–17.
- (38) Hohenberg, P.; Kohn, W. Inhomogeneous Electron Gas. *Phys. Rev.* **1964**, *136*, B864.
- (39) Fang, W.-H. Ab Initio Determination of Dark Structures in Radiationless Transitions for Aromatic Carbonyl Compounds. *Acc. Chem. Res.* **2008**, *41* (3), 452–457.
- (40) Chen, S.-L.; Marino, T.; Fang, W.-H.; Russo, N.; Himo, F. Peptide Hydrolysis by the Binuclear Zinc Enzyme Aminopeptidase from *Aeromonas proteolytica*: A Density Functional Theory Study. *J. Phys. Chem. B* **2008**, *112* (8), 2494–2500.
- (41) Liu, X.-Y.; Chen, W.-K.; Fang, W.-H.; Cui, G. Nonadiabatic Dynamics Simulations for Photoinduced Processes in Molecules and Semiconductors: Methodologies and Applications. *J. Chem. Theory Comput.* **2023**, *19* (23), 8491–8522.
- (42) Jacobson, L. D.; Bochevarov, A. D.; Watson, M. A.; Hughes, T. F.; Rinaldo, D.; Ehrlich, S.; Steinbrecher, T. B.; Vaitheeswaran, S.; Philipp, D. M.; Halls, M. D.; Friesner, R. A. Automated Transition State Search and Its Application to Diverse Types of Organic Reactions. *J. Chem. Theory Comput.* **2017**, *13* (11), 5780–5797.
- (43) Fang, W.-H. Ab Initio Study of the Triple-Proton-Transfer Reactions of Ground and Excited States of 7-Hydroxyquinoline in Methanol Solution. *J. Am. Chem. Soc.* **1998**, *120* (30), 7568–7576.
- (44) Polubesova, T.; Chen, Y.; Navon, R.; Chefetz, B. Interactions of Hydrophobic Fractions of Dissolved Organic Matter with Fe<sup>3+</sup>- and Cu<sup>2+</sup>-Montmorillonite. *Environ. Sci. Technol.* **2008**, *42* (13), 4797–4803.
- (45) Chakrabarty, A.; Schellman, J. A.; Baldwin, R. L. Large Differences in the Helix Propensities of Alanine and Glycine. *Nature* **1991**, *351* (6327), 586–588.
- (46) Huyghues-Despointes, B. M. P.; Scholtz, J. M.; Baldwin, R. L. Effect of a Single Aspartate on Helix Stability at Different Positions in a Neutral Alanine-based Peptide. *Protein Sci.* **1993**, *2* (10), 1604–1611.
- (47) Ghazanfari, S.; Han, Y.; Xia, W.; Kilin, D. S. First-Principles Study on Optoelectronic Properties of Fe-Doped Montmorillonite Clay. *J. Phys. Chem. Lett.* **2022**, *13*, 4257–4262.
- (48) Hafner, J. Ab-initio Simulations of Materials Using VASP: Density-functional Theory and Beyond. *J. Comput. Chem.* **2008**, *29* (13), 2044–2078.
- (49) Perdew, J. P.; Burke, K.; Ernzerhof, M. Generalized Gradient Approximation Made Simple. *Phys. Rev. Lett.* **1996**, *77* (18), 3865–3868.
- (50) Himmetoglu, B.; Floris, A.; De Gironcoli, S.; Cococcioni, M. Hubbard-corrected DFT Energy Functionals: The LDA+ U Description of Correlated Systems. *Int. J. Quantum Chem.* **2014**, *114* (1), 14–49.
- (51) Henkelman, G.; Jónsson, H. Improved Tangent Estimate in the Nudged Elastic Band Method for Finding Minimum Energy Paths and Saddle Points. *J. Chem. Phys.* **2000**, *113* (22), 9978–9985.
- (52) Henkelman, G.; Uberuaga, B. P.; Jónsson, H. A Climbing Image Nudged Elastic Band Method for Finding Saddle Points and Minimum Energy Paths. *J. Chem. Phys.* **2000**, *113* (22), 9901–9904.
- (53) Liu, Y.; Cui, G.; Fang, W.-H. Automated Search of Minimum-Energy Conical Intersections with Projected Metadynamics. *J. Chem. Phys.* **2025**, *162* (5), 1–10.
- (54) Han, Y.; Hobbie, E. K.; Kilin, D. S. First-Principles Molecular Dynamics of Monomethylhydrazine and Nitrogen Dioxide. *J. Phys. Chem. Lett.* **2019**, *10* (10), 2394–2399.
- (55) Arrhenius, S. Über Die Reaktionsgeschwindigkeit Bei Der Inversion von Rohrzucker Durch Säuren. *Zeitschrift für Phys. Chemie* **1889**, *4U* (1), 226–248.
- (56) Kooij, D. M. Über Die Zersetzung Des Gasförmigen Phosphorwasserstoffs. *Zeitschrift für Phys. Chemie* **1893**, *12U* (1), 155–161.
- (57) Laidler, K. J. The Development of the Arrhenius Equation. *J. Chem. Educ.* **1984**, *61* (6), 494.
- (58) Trautz, M. Der Temperaturkoeffizient Chemischer Reaktionsgeschwindigkeiten. II. Die Physikalische Bedeutung Der Chemischen Reaktionsgeschwindigkeit in Gasen Und Ihre Vorausberechnung Ans Rein Thermischen Daten Der Beteiligten Stoffe. *Zeitschrift für Phys. Chemie* **1909**, *66U* (1), 496–511.
- (59) Tyagi, V. P. *Essential Chemistry XII*; Ratna Sagar: New Delhi, India, 2009.
- (60) Tang, W.; Sanville, E.; Henkelman, G. A Grid-Based Bader Analysis Algorithm without Lattice Bias. *J. Phys.: Condens. Matter* **2009**, *21* (8), 084204.
- (61) Shafei, L.; Adhikari, P.; Ching, W.-Y. DFT Study of Electronic Structure and Optical Properties of Kaolinite, Muscovite, and Montmorillonite. *Crystals* **2021**, *11* (6), 618.
- (62) Meierhenrich, U. *Amino Acids and the Asymmetry of Life: Caught in the Act of Formation*; Springer: Berlin, Germany, 2008; DOI: 10.1007/978-3-540-76886-9.
- (63) Ball, D. W.; Hill, J. W.; Scott, R. J. *The Basics of General, Organic, and Biological Chemistry*; Open Textbook Library: Minneapolis, MN, 2011.
- (64) Pathak, A. K. Stabilizing the Zwitter-Ionic Form of Amino Acids in the Gas Phase: An Ab Initio Study on the Minimum Number of Solvents and Ions. *Chem. Phys. Lett.* **2014**, *610*, 345–350.
- (65) Forde, A.; Ghosh, D.; Kilin, D.; Evans, A. C.; Tretiak, S.; Neukirch, A. J. Induced Chirality in Halide Perovskite Clusters through Surface Chemistry. *J. Phys. Chem. Lett.* **2022**, *13* (2), 686–693.
- (66) Forde, A.; Evans, A. C.; Nie, W.; Tretiak, S.; Neukirch, A. J. Influence of Material Properties on Surface Chemistry Induced Circular Dichroism in Halide Perovskite: Computational Insights. *Nano Lett.* **2024**, *24* (30), 9276–9282.
- (67) Meisner, J.; Kamp, L.; Thi, W.-F.; Kästner, J. The Role of Atom Tunneling in Gas-Phase Reactions in Planet-Forming Disks. *Astron. Astrophys.* **2019**, *627*, A45.
- (68) Waxman, D.; Leggett, A. J. Dissipative Quantum Tunneling at Finite Temperatures. *Phys. Rev. B* **1985**, *32* (7), 4450.
- (69) Kuhnen, C. A.; Dall'Oglio, E. L.; de Sousa, P. T., Jr. Quantum Tunneling Contribution to the Activation Energy in Microwave-Induced Reactions. *J. Phys. Chem. A* **2017**, *121* (30), 5735–5747.